iScience

CellPress
OPEN ACCESS

Article

A high-performance triboelectric-electromagnetic hybrid wind energy harvester based on rotational tapered rollers aiming at outdoor IoT applications

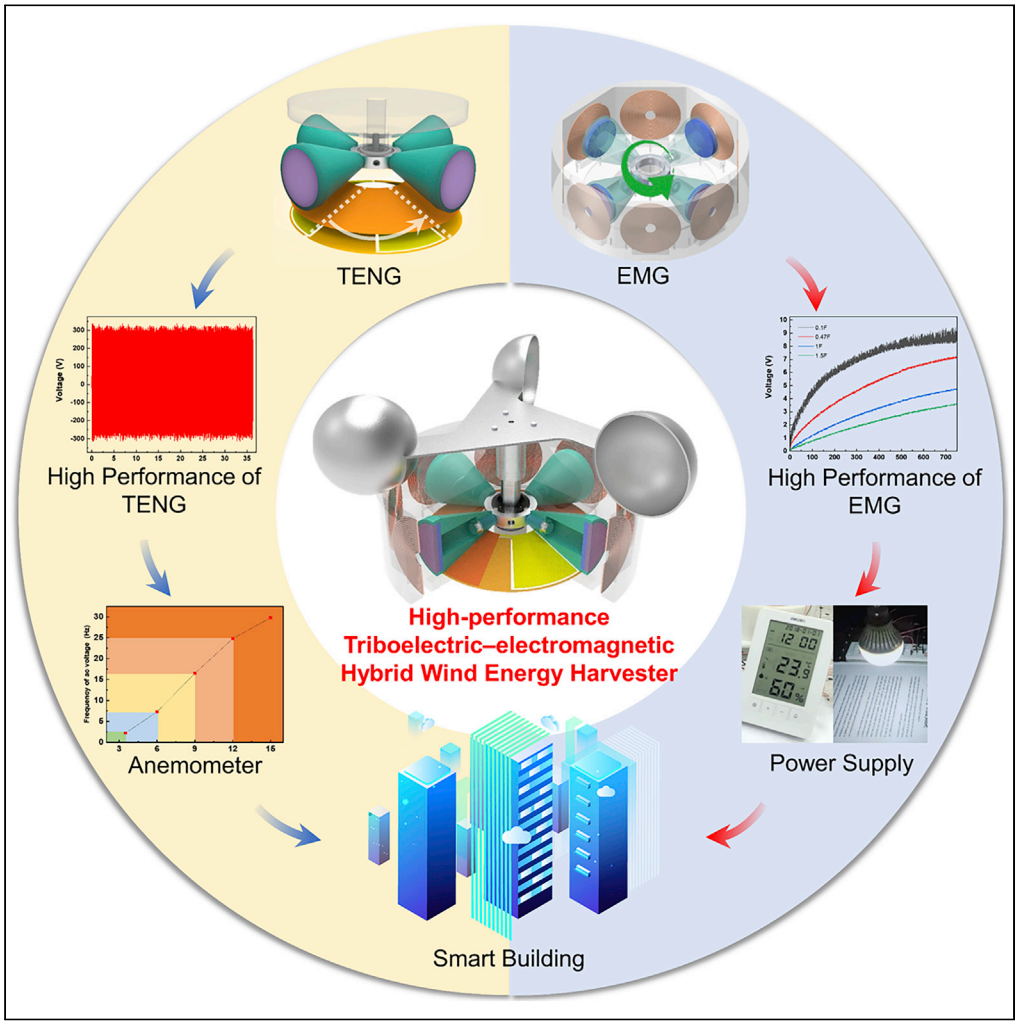

Yan Fang, Tianyi Tang, Yunfei Li, ..., Lining Sun, Huicong Liu, Chengkuo Lee

yangzhan@suda.edu.cn (Z.Y.)
hcliu078@suda.edu.cn (H.L.)
elelc@nus.edu.sg (C.L.)

Highlights

A triboelectric-electromagnetic hybrid generator based on tapered rollers is proposed

The high-performance WEH has been systematically optimized and tested

A self-powered anemometer system has been successfully established

The WEH shows bright prospect in future IoT applications

Fang et al., iScience 24, 102300
April 23, 2021
https://doi.org/10.1016/j.isci.2021.102300

iScience

CellPress
OPEN ACCESS

Article

A high-performance triboelectric-electromagnetic hybrid wind energy harvester based on rotational tapered rollers aiming at outdoor IoT applications

Yan Fang,[1,6] Tianyi Tang,[1,6] Yunfei Li,[2,6] Cheng Hou,[1] Feng Wen,[3,4,5] Zhan Yang,[1,*] Tao Chen,[1] Lining Sun,[1] Huicong Liu,[1,7,*] and Chengkuo Lee[3,4,5,*]

SUMMARY

This article proposed a high-performance triboelectric-electromagnetic hybrid wind energy harvester (WEH). By adopting the revolution and rotation movements of tapered rollers, which serve as both the rotor of the electromagnetic generator (EMG) part and freestanding layers of the triboelectric nanogenerator (TENG) part, the WEH can work as a sustainable power source and a self-powered wind speed sensor. When the wind speed is 12 m/s, super-high open-circuit voltage peaks of 47.4 and 683 V can be achieved by the EMG and TENG, respectively, corresponding to the high-power outputs of 62 and 1.8 mW. It was demonstrated that the WEH can easily light up over 600 red light-emitting diodes and even a 5-W globe light. A self-powered wireless temperature and humidity sensing network was also systematically demonstrated. In summary, the proposed WEH exhibits bright future toward IoT applications, such as in border detection, smart buildings, and so on.

INTRODUCTION

With the wide spread of Internet of Things (IoTs) and further development of embedded technology, the application of wireless sensor networks is becoming more and more popular in recent years (Li et al., 2016; Chen et al., 2018, 2019; Ryu et al., 2019). Numerous sensor nodes are conventionally powered by batteries, which intrinsically suffer from the problem of limited lifetime (Chen et al., 2015b). Considering the challenges of worldwide energy crisis and related environmental issue (Chu and Majumdar, 2012; Armstrong et al., 2016), power supply turns to be a bottleneck problem for the long-term application of IoTs. To crack this hard nut, remarkable efforts have been made over the last decades. Harvesting renewable energy, including but not limited to solar (Oh et al., 2012), wind (El-Askary et al., 2015; Wen et al., 2016; Kosunalp, 2017; Orrego et al., 2017), rain drop (Zheng et al., 2014), and blue energy (Li et al., 2019; Chen et al., 2020) from the ambient environment, and then converting it into electricity to provide power supply to IoT applications, is of utmost significance to the sustainable development of modern society. Wind energy is widely known as a kind of renewable energy, which is ubiquitous in the wildness (Cheng and Zhu, 2014; Wang et al., 2016; Lai et al., 2019), and wind energy harvester (WEH) is considered as an ideal solution to sustainable power supply to smart sensors in IoT applications (Bethi et al., 2019; Wang et al., 2020). Generally speaking, the existing WEHs can be divided into two types: vibrational and rotational. The vibrational WEHs convert wind energy into the vibration energy of an elastic structure by utilizing the effects of fluttering (Li and Lipson, 2009; Zhao et al., 2016; Liu et al., 2018; Lin et al., 2019), galloping (Fei et al., 2012; Zhou et al., 2018), vortex shedding (Weinstein et al., 2012; Chen et al., 2016), and resonance (Wang et al., 2014; Zhang et al., 2015). The rotational WEHs convert wind energy into the rotation energy of rotators based on the piezoelectric (Fu and Yeatman, 2015a, 2015b; Zhang et al., 2017), triboelectric (Chen et al., 2015c; Wen et al., 2015; Ahmed et al., 2017; Kim et al., 2018), and electromagnetic (Weimer et al., 2006; Liu et al., 2019) effects, independently or in combination (Zhong et al., 2015; Chen et al., 2015a; Guo et al., 2016; Cao et al., 2017; Yang et al., 2018, 2019; Hao et al., 2019). Compared with the vibrational WEHs, the rotational WEHs are inherent with the characters of higher power output, longer working life, and more stable performance. From the aspect of energy conversion effects, triboelectric nanogenerators (TENGs) (Wang et al., 2012; Lin et al., 2013, 2014; Li et al., 2015) show great advantages of high voltage, small size, light weight, and easy fabrication (Wang, 2013; Wang et al., 2015; Liu et al., 2017; Cheng et al., 2019), whereas electromagnetic generators (EMGs) (Spreemann et al., 2006; A. Bansal et al., 2009;

[1]School of Mechanical and Electric Engineering, Jiangsu Provincial Key Laboratory of Advanced Robotics, Soochow University, Suzhou 215123, China

[2]State Key Laboratory of Robotics and System, Harbin Institute of Technology (HIT), Harbin 150001, China

[3]Department of Electrical & Computer Engineering, National University of Singapore, 4 Engineering Drive 3, Singapore 117576, Singapore

[4]National University of Singapore Suzhou Research Institute (NUSRI), Suzhou Industrial Park, Suzhou 215123, China

[5]Center for Intelligent Sensors and MEMS, National University of Singapore, E6 #05-11F, 5 Engineering Drive 1, Singapore 117608, Singapore

[6]These authors contributed equally

[7]Lead contact

*Correspondence: yangzhan@suda.edu.cn (Z.Y.), hcliu078@suda.edu.cn (H.L.), elelc@nus.edu.sg (C.L.)

https://doi.org/10.1016/j.isci.2021.102300

Halim et al., 2018) hold superior in high currents, low cost, compact structure, and excellent stability (Zhao et al., 2019b; Hou et al., 2019). Hence, it is rational to combine TENG with EMG to draw on each other's strengths.

Numerous researches show the hybridization road of energy harvesting from single effect to multi-effects. After a wind cup-driven rotational TENG was proposed by Xie et al. (2013), Zhao et al. proposed a triboelectric-electromagnetic hybrid nanogenerator (Zhao et al., 2019a). Based on the hybridization of triboelectric and electromagnetic effects, a well-packaged WEH was proposed by Fan et al. (2020) to power a commercial hygrothermograph or a wireless environmental monitoring system even in harsh environment. Zhang et al. demonstrated a rotating-disk-based hybridized nanogenerator to effectively harvest energy from wind generated by a moving vehicle through the tunnel (Zhang et al., 2016), which can be utilized as a self-powered wireless sensor for traffic volume monitoring in the remote mountain area. Cao et al. reported a rotating-sleeve triboelectric-electromagnetic hybrid nanogenerator (Cao et al., 2017), which was capable of lighting dozens of light-emitting diodes (LEDs) as well as powering an electronic watch under blowing wind. He et al. introduced a rotary cylinder-based nanogenerator, by hybridizing a TENG and an EMG (He et al., 2019), which can operate as a self-powered counter and timer for potential speed detecting. Guo et al. designed a pinwheel-like nanogenerator by coupling triboelectric and electromagnetic effects (Guo et al., 2019), which not only can charge capacitors but also can power many portable electronic devices even in a rather low wind speed. As energy harvesting technology is booming for decades, although some WEHs have the potential ability to convert the wind energy into electricity for powering the self-powered wireless sensor nodes in the wild, there is still a long way to go to enhance the output performance. Still on this purpose, a high-performance triboelectric-electromagnetic hybrid WEH for wind energy harvesting is proposed, which can be used as not only a high-output power source but also a self-powered anemometer. The hybrid WEH consists of an EMG part and a TENG part. Driven by the rotating wind cup, the nylon tapered rollers together with magnets begin to rotate, which not only induces an electric current in the surrounding coils but also enables the bottom fluorinated ethylene propylene (FEP) layer to generate electricity between electrodes.

RESULTS AND DISCUSSION

Device structure

The device structure of the proposed WEH is schematically illustrated in Figure 1A, which consists of a horizontal conical TENG part and a vertical cylindrical EMG part. Both the TENG and EMG are composed of stators and rotators. For the stator of the TENG, a copper foil was first cut into interdigital electrode pattern and then adhered to the conical surface of the acrylic (PMMA) substrate. A layer of FEP film was finally laminated on the electrodes to work as one triboelectric material. Four hollow tapered nylon rollers as the other triboelectric material were used as the rotator of the TENG. For the EMG, four penny-shaped polarized magnets were fixed inside the bottom hole of the hollow tapered rollers serving as the rotator. Aligned with the magnets, eight synclastic twined copper coils were uniformly embedded on the octagonal side wall of PMMA frame serving as the stator of the EMG. A wind cup was connected with a PMMA top cover through a shaft to convert wind flow into the revolution and rotation movement of the four tapered rollers. In order to enhance the movement of tapered rollers, a ball bearing was fixed at the end of the shaft. Once the relative movement between the rotators and stators occurs, both charge transfer of the TENG and flux change of the EMG will produce electrical output periodically. Figure 1B shows the photographs of (1) the stator part, (2) the rotator part, and (3) the assembled WEH.

In order to further illustrate the advantages of tapered roller structure, the comparisons of potential distribution and equivalent stress between tapered, cylindrical, and spherical rollers are shown in Figures S1 and S2, respectively. When the external conditions are consistent, the tapered roller shows better potential distribution and mechanical properties than the other two. In addition, the diameter of the inner and outer rings of the tapered roller can be adjusted to ensure only pure rolling of the roller with the base, as shown in Figure S3. However, the contact between the cylindrical roller and the base is similar to that of the spherical roller, which could induce sliding friction with the base and affect the rotation of the device. Therefore, the tapered roller structure enables the device to work more efficiently.

Working principle and simulation

As shown in Figure 2A, the working mechanism of the EMG is based on the fundamental principle of Faraday's law of electromagnetic induction (Zhang et al., 2014). Briefly speaking, as long as the magnetic flux

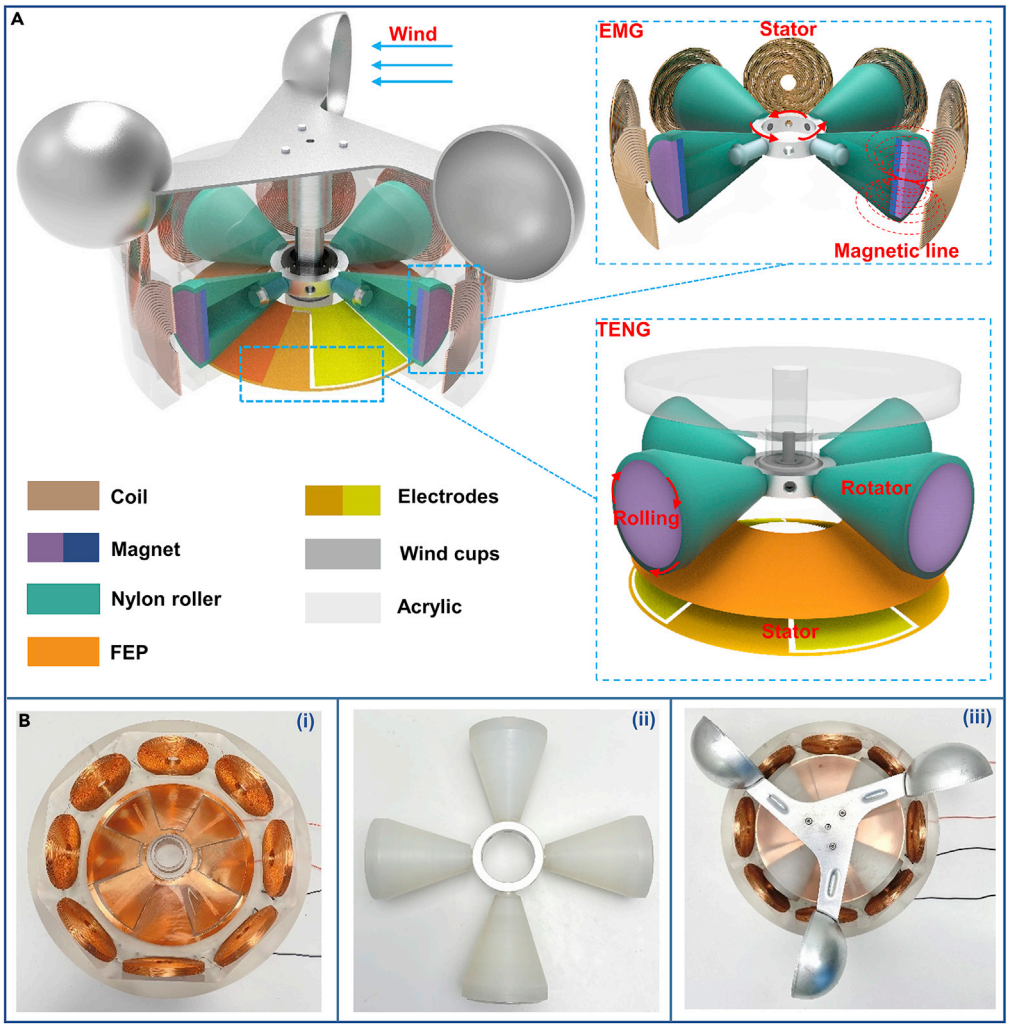

Figure 1. Device structure of the WEH

(A) Structural schematic of the WEH.

(B) Photographs of the (i) rotator part, (ii) the stator part, and (iii) the assembled WEH.

passing through the closed coil changes, the induced current will be generated and the corresponding open-circuit voltage and short-circuit current can be represented as:

$$E_{EMG} = \frac{d\Phi}{dt} = N\frac{SdB}{dt} \quad \text{Equation (1)}$$

$$I_{EMG} = \frac{E_{EMG}}{R} \quad \text{Equation (2)}$$

where N is the number of the coil turns, Φ is the magnetic flux, t is the time, B is the magnetic flux density, S is the area of the coil, and R is the resistance of the coil.

To gain a more quantitative understanding of the proposed working principle of the EMG, finite element analysis was employed to calculate the magnetic flux density contour of the whole volume and the magnetic induction line distribution of the midsection via JMAG, as displayed in Figures 2B and 2C, respectively. There are two critical positions between the rotational magnets and fixed coils. One is the original position where each magnet is well-aligned with a coil as shown in Figures 2B(i) and 2C(i), and the other is the intermediate position where each magnet is just located in the middle of two adjacent coils as shown in Figures 2B(ii) and 2C(ii). Figure 2D shows the magnetic flux density with respect to the rotation angle of magnets, and Figure 2E displays the induced circuit voltage against EMG part. In the original position,

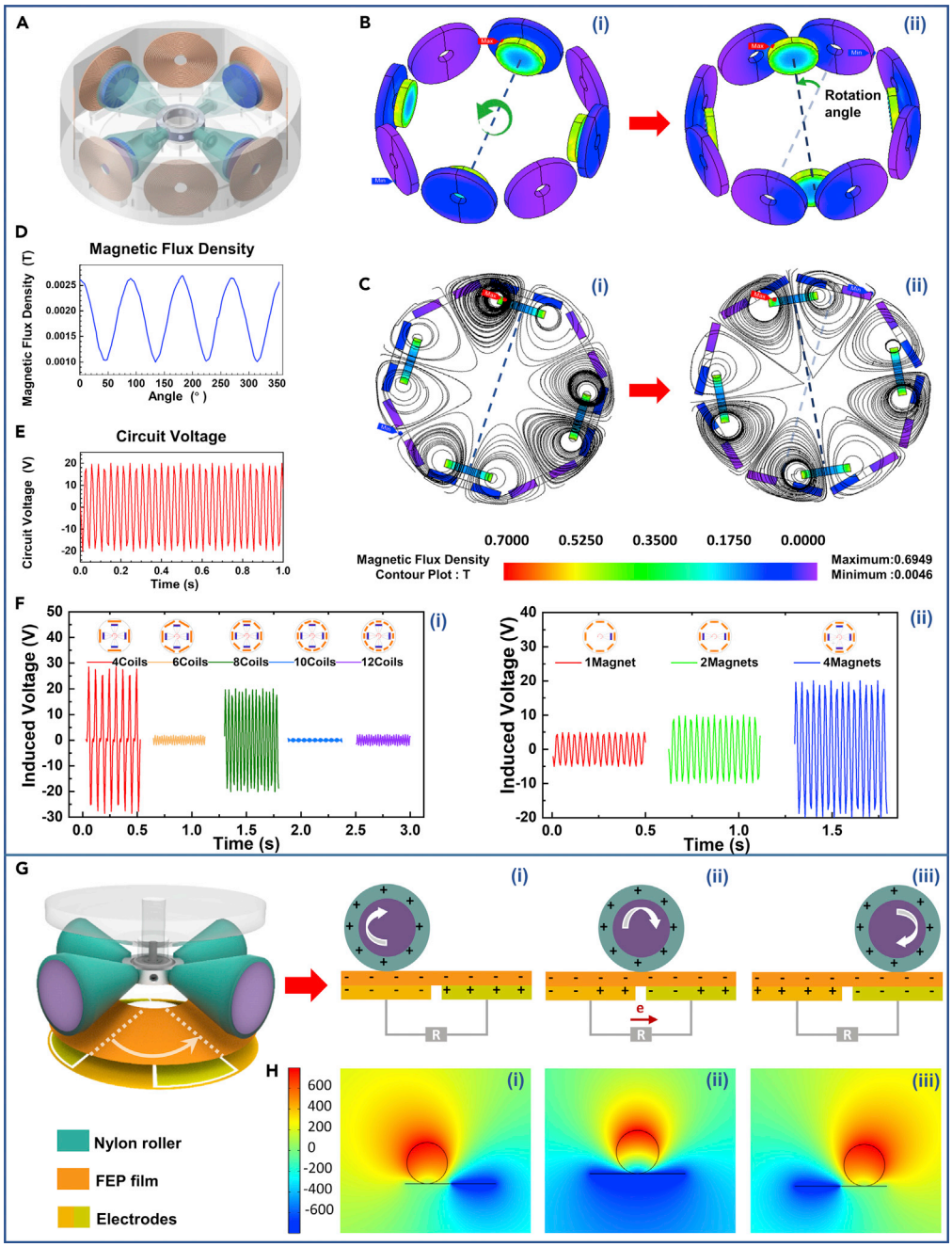

Figure 2. Working mechanisms of the EMG and TENG

(A) Basic model of the EMG.

(B) Magnetic flux density contour of the whole volume: (i) original position; (ii) intermediate position.

(C) Magnetic induction line distribution of the midsection: (i) original position; (ii) intermediate position.

(D) The magnetic flux density with respect to the rotation angle of magnets simulated by JMAG software.

(E) Induced circuit voltage against EMG simulated via JMAG software.

(F) The numerical calculation results about induced voltage of the EMG with different arrangements of coils and magnet number.

(G) Basic model of the TENG part and corresponding schematic illustrations of the charge distribution: (i) initial state; (ii) intermediate state; (iii) the third state.

(H) Potential distribution between the paired electrodes simulated via COMSOL: (i) initial state; (ii) intermediate state; (iii) the third state.

the magnetic flux through the coil is maximum and there is no current in the coil. As the magnets rotate anticlockwise with taper rollers, the magnetic flux in the coils declines first, which will lead to an induced positive current consequently. Until the magnets rotate to the intermediate position, the magnetic flux reaches a minimum. As the magnets continue rotating and recover to the original position eventually, the magnetic flux in the coil then increases gradually, which will lead to negative current subsequently.

A more in-depth simulation analysis was also carried out to optimize parameters of the EMG part under the same rotation speed of 240 r/min. In this section, the arrangement of coil and the magnet number were supposed to play a considerable role in the output performance of the EMG, because the electromagnetic induction process relies on the number of the coil turns and the rate of the change in magnetic flux. For this purpose, the side wall of PMMA frame was evenly distributed with 4, 6, 8, 10, and 12 coils in different outer diameters of 60, 53, 46, 39, and 32 mm correspondingly, with a constant magnet number of 4. The magnetic flux density contour of the whole volume, the magnetic induction line distribution of the midsection, and the detailed induced voltage of the EMG are shown in Figure S4. Figure 2F(i) depicts the series-induced voltages of all these five arrangements of coils. It is also found that the induced voltage decreases as the coil number increases from 4, 8 to 12, which are the integral multiples of the magnet number 4, since the turns of coil are actually decreased from 2,220 to 980. When the coil number is 8, the induced voltage is lower than the case when the coil number is 4; however, the average output power is much higher than that case. Figure S6 is the output work curve of the EMG within 1 s, and its slope represents the average power of the EMG. So considering the power output, the arrangement of 8 coils is a favorable choice. It is worth mentioning that the induced voltage tends to be at a remarkable low level when the coil number is 6 and 10, which is because the direction of the induced current in different coils is inconsistent in these two arrangements. In other words, there is an integer proportional correspondence between the coil number and the magnet number. For the purpose of avoiding that inconsistency, the magnet number can only be a divisor of 8, which is 8, 4, 2, and 1. The numerical calculation results about induced voltage of the EMG with different magnet numbers are presented in Figure 2F(ii). Figure S5 shows the corresponding magnetic flux density contour of the whole volume, the magnetic induction line distribution of the midsection, and the detailed induced voltage of the EMG. It can be observed that the induced voltage increases as the coil number increases from 1 to 8. However, in subsequent experiments, when the magnet number is 8, the magnetic force is so strong that the bottoms of the tapered rollers are attracted together, making the rollers unable to rotate. Therefore the magnet number was optimized as 4 in the device.

Figure 2G shows the basic model of the TENG part, and the working mechanism is based on the coupling effect of triboelectrification and electrostatic induction. Figures 2G(i)–2G(iii) illustrates the following three consecutive states of a tapered roller between a pair of interdigital electrodes. When the tapered nylon roller and the FEP film are brought into contact, surface charge transfer takes place due to the triboelectrification effect and electrons are injected from the nylon roller into the FEP film because of the higher electron affinity of FEP than nylon. According to the charge conservation law, an equal amount of negative and positive charges would be generated on the FEP film and nylon roller, respectively. At this moment, the tapered nylon roller can be regarded as a uniform positive electric roller. Once the roller was approaching to and/or departing from the two interdigital electrodes, it would create an asymmetric charge distribution via induction in the media causing the electrons to flow between the two electrodes to balance the local potential distribution. The oscillation of the electrons between the paired electrodes in response to the motion of tapered rollers produces an AC output, which forms the fundamental processes of converting mechanical energy into electricity. According to the capacitor model (Zhang et al., 2014), the open-circuit voltage and the short-circuit current of the TENG can be represented as

$$E_{TENG} = \frac{Q}{C} \quad \text{Equation (3)}$$

$$I_{EMG} = \frac{dQ}{dt} \quad \text{Equation (4)}$$

where Q is the triboelectric charge capacity and C is the capacitance between electrodes.

The variations of electric potential distribution between the paired electrodes for three critical positions are also simulated via COMSOL as displayed in Figure 2H. At the initial state in Figure 2H(i), the nylon roller is on the left electrode spaced by the FEP film, where corresponds to a maximum electrical potential on the left electrode and a minimum potential on the right electrode. Thus a maximized electrical potential deference between the two electrodes is generated, resulting in a maximum open-circuit voltage. Then the

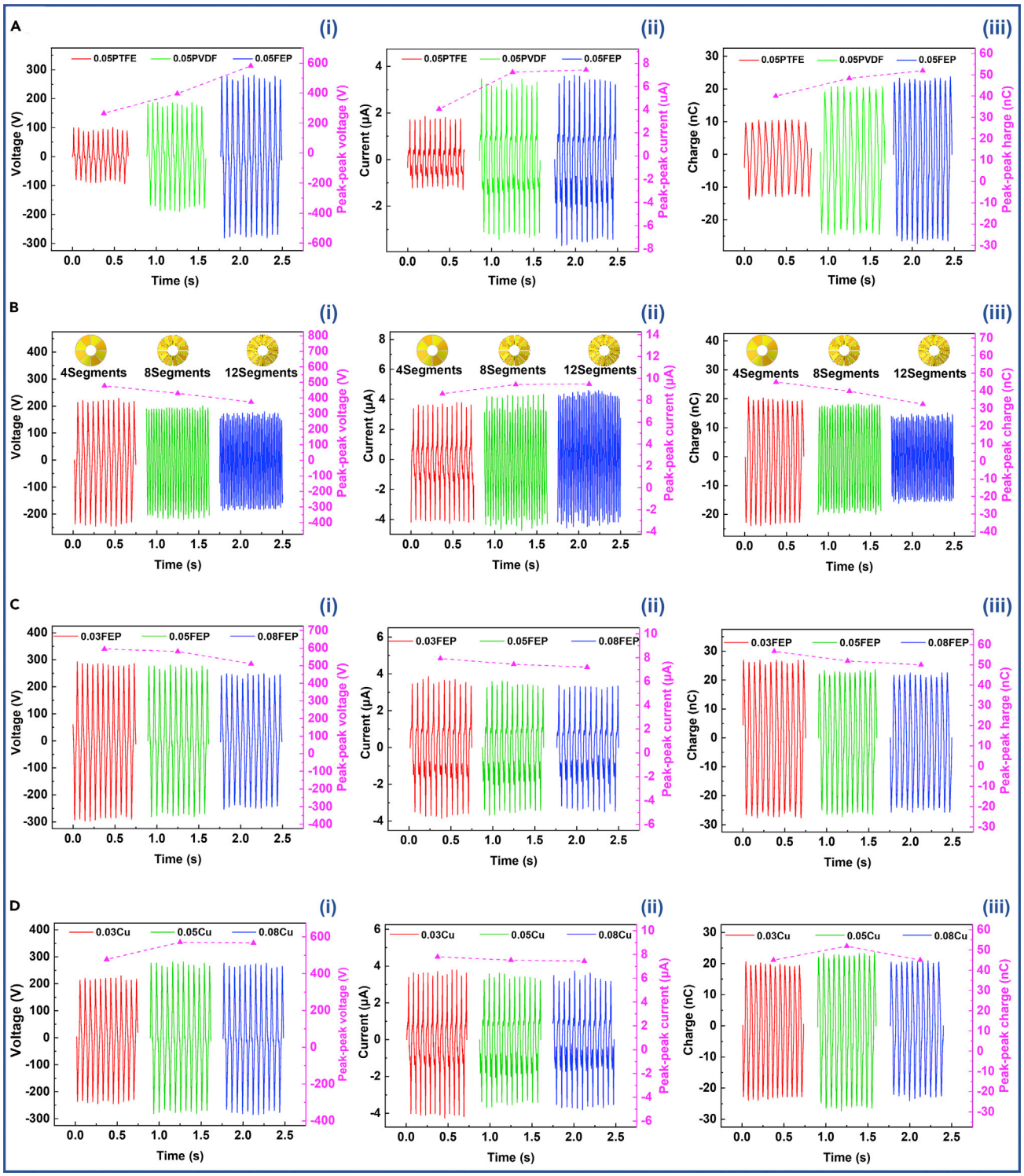

Figure 3. Optimization of the output performance of the TENG

(A) Output performance of the TENG with Cu electrode of different materials of dielectric film (FEP, PTFE, PVDF) at the wind speed of 12 m/s: (i) open-circuit voltage; (ii) short-circuit current; (iii) transferred charge.

(B) Output performance of the TENG with Cu electrode of different segment numbers (4, 8. and 12) at the wind speed of 12 m/s: (i) open-circuit voltage; (ii) short-circuit current; (iii) transferred charge.

Figure 3. *Continued*

(C) Output performance of the TENG with the FEP film of different thickness (30, 50, and 80 μm) at the wind speed of 12 m/s: (i) open-circuit voltage; (ii) short-circuit current; (iii) transferred charge.

(D) Output performance of the TENG with Cu electrode of different thickness (30, 50, and 80 μm) at the wind speed of 12 m/s: (i) open-circuit voltage; (ii) short-circuit current; (iii) transferred charge.

nylon roller starts to rotate clockwise, the open-circuit voltage starts to diminish till the intermediate state between the two electrodes in Figure 2H(ii), where it turns to zero. Further rotation beyond this position will result in a reversely established open-circuit voltage and is maximized at the third state in Figure 2H(iii).

Output characterization of the hybrid WEH

To begin with, a series of experiments were carried out to optimize the output performance of the TENG part under the wind speed of 12 m/s, including the material of dielectric film, the segment number of each electrode, and the thickness of the dielectric film and the electrodes. First, the output performance of dielectric films made of different materials (PTFE, PVDF, FEP) was investigated systematically. Figures 3A(i)–3A(iii) depict the open-circuit voltage, short-circuit current, and transferred charge of three different dielectric films. It can be noted from Figure 3A that the dielectric film made of FEP film has the highest output, which is probably because that FEP has a lower dielectric constant than PTFE and PVDF, resulting in a lower capacitance between electrodes and eventually leading to a higher voltage output according to Equation 3. Second, three types of TENGs with different segment numbers (4, 8, and 12) of electrodes were taken into consideration. According to the decreasing trend of the potential distribution as the roller size decreases in Figure S7, the size of the roller was retained when increasing the number of electrode segments. Figures 3B(i)–3B(iii) demonstrate the open-circuit voltage, short-circuit current, and transferred charge of the TENG with those different types. It can be found that the frequency of the output signals increases exponentially with the doubled or tripled segmentation. It can also be noted that the transferred charge of the TENG decreases obviously as the segment number increases from 4, 8 to 12, which may result from the lower magnitude of polarization due to more sharp edges for finer segments. As the open-circuit voltage of the TENG is directly related to the transferred charges between the electrode pairs according to Equation 3, the open-circuit voltage of the TENG exhibits an obvious declining trend with the increase of segment number. On the contrary, the short-circuit current shows a slightly ascending trend as the segment number increases, mainly owing to the obvious increase of the charge transferring rate between the electrodes from fully contact to fully separation according to Equation 4. Third, the effect of the thickness of FEP film (30, 50, and 80 μm) on the output performance of the TENG was studied subsequently. Figures 3C(i)–3C(iii) illustrate the open-circuit voltage, short-circuit current, and transferred charge of the TENG with different thicknesses of FEP films, indicating that there is only a minor decrease in those three output signals of the TENG when the FEP film gets thicker, probably on account of the vertical gap between the triboelectric surface and the electrode plane. It is worth mentioning that when the thickness of FEP is 30 μm, the electric output of the film was significantly reduced due to the severe wear. Hence, the thickness of the FEP is determined as 50 μm after a trade-off between output performance and service lifetime. Last, we researched the output performance of the TENG with different thickness of the Cu electrodes (30, 50, and 80 μm). As displayed in Figures 3D(i)–3D(iii), the open-circuit voltage, short-circuit current, and transferred charge of the TENG are relatively larger when the thickness of Cu electrode is 50 μm.

The influence of the wind speed on the output performance of the EMG and TENG is then investigated systemically. As the wind speed increases from 3.5 to 15 m/s, the open-circuit voltage of the EMG increases gradually from 3.14 to 47.4 V in Figure 4A, which is due to the acceleration of change in magnetic flux as the increase of rotation speed. Figure 4B shows the open-circuit voltage of the TENG increases gradually from 71 to 683 V with the wind speed increasing from 3.5 to 12 m/s and then remains saturated at 12 m/s. When the wind speed is high enough, the triboelectric friction will no longer be enhanced, and that is why contact surface area and triboelectric charge density will hardly increase and the open-circuit voltage approaches a constant. Figures 4C and 4D depicted the output voltages and power against different external load resistances at the wind speed of 12 m/s. The output voltages of both EMG and TENG grow gradually with the increase of load resistance. The corresponding output power of both reach maximum values and then turn to decrease until the optimal matched load resistances. The output power of EMG reaches the climax of 62 mW at the external load of 660 Ω, which corresponds to a volume output power density of 72.1 W/m^3, whereas the maximum output power of TENG is achieved as 1.8 mW at the external load of 60 MΩ, which corresponds to an output power density of 2.7 W/cm^2. From the aforementioned data, it can be concluded

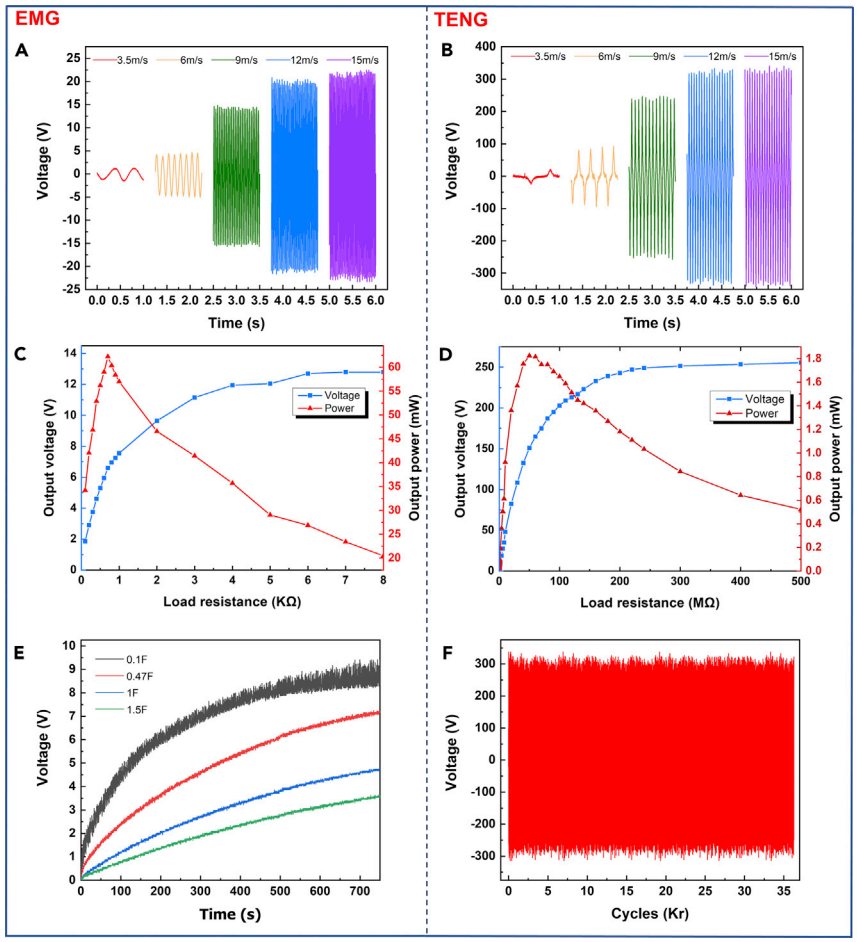

Figure 4. Output characterization of the WEH

(A) Open-circuit voltage of the TENG under different wind speeds.

(B) Open-circuit voltage of the EMG under different wind speeds.

(C) Output voltage and power of the TENG with different external load resistances at the wind speed of 12 m/s.

(D) Output voltage and power of the EMG with different external load resistances at the wind speed of 12 m/s.

(E) Measured voltages of different supercapacitors in F-level charged by EMG at the wind speed of 12 m/s.

(F) Measured voltages of the TENG run for ~35,000 cycles at the wind speed of 12 m/s.

that the output characteristics of TENG generates higher voltage but with larger matched load resistance, whereas the EMG generates lower voltage but with relatively higher power output. For a more intuitive comparison of high performance of our device, relevant information is listed as Table 1.

The charging capability of the EMG is investigated by connecting a full-wave rectifying bridge to charge different supercapacitors of 0.1, 0.47, 1, and 1.5 F, respectively. As the charging curves of the EMG shown in Figure 4E, a supercapacitor of 1.5 F can be charged to 3 V within 10 min, which implies its excellent charging capacity. For testing the stability of TENG, the device with an optimized structure has been continuously run for ~35,000 cycles, and the result indicates that the generated open-circuit voltage of ~640 V did not have an obvious decay after those many cycles, as shown in Figure 4F.

Application demonstration of the hybrid WEH

To demonstrate the potential application toward a practical power source, the WEH was first operated to power up lighting electronic, such as an array of LEDs and even a 5-W globe light. It can be seen from Figure 5B(i) (Video S1) that the individual EMG can easily light up (ii) 360 red LEDs connected in parallel, whereas the individual TENG can visibly light up (iii) 240 red LEDs connected in series. As demonstrated

Table 1. Comparison and summary of the reported wind energy harvesters with various output performances.

Reference	Harvester	Output power	Rotation speed	Power density ($W/m^3 \cdot rpm$)
(Xie et al., 2013)	TENG	12 mW	180 rpm[a]	0.21[b]
(Zhao et al., 2019a, 2019b)	EMG and TENG	10.8 mW	100 rpm	0.24[b]
(Fan et al., 2020)	EMG and TENG	18.96 mW	420 rpm[a]	0.05[b]
(Zhang et al., 2016)	EMG and TENG	17.5 mW	1,000 rpm	0.06[b]
(Cao et al., 2017)	EMG and TENG	12.7 mW	250 rpm	0.05[b]
(He et al., 2019)	EMG and TENG	1.8 mW	150 rpm	0.08[b]
(Guo et al., 2019)	EMG and TENG	3.61 mW	300 rpm[a]	0.04[b]
This work	**EMG and TENG**	**62 mW**	**267 rpm**	**0.27**

[a]The rotation speed is estimated according to the frequency of AC voltage given in the article.
[b]The volume is estimated according to the dimensional parameters given in the article.

in Figure 5C, a 5-W globe light was lit up instantly and capable of providing sufficient illumination in complete darkness. Together with solar power generation, the WEH shows potential talent to be used as a supplementary power source for wind-solar complementary generation mode in outdoor lighting as illustrated in Figure 5A.

Owing to the development of fifth-generation (5G) and big data, smart buildings have become the ideal living and office spaces pursued by government agencies, companies, enterprises, and residential building. Each smart building has a number of sensing nodes that form a network in the city and feedback real-time sensing information including temperature, wind speed, and humidity. The hybrid WEH can not only convert wind energy into electrical energy as power supply to sensors, microprocessors, and wireless transmission modules but also as a self-powered anemometer due to the linear relationship between frequency of AC voltage of TENG and wind speed. As schematically illustrated in Figure 6A, the WEH is applicable for smart building and other IoT applications. On the one hand, the device can be used to activate a temperature and humidity (T&H) sensing node and a hygrothermograph simultaneously in Figure 6B(i), which can transmit signals to a computer interface via Bluetooth with the aid of a 6,800-μF capacitor. Figure 6B(iii) shows the charging-discharging curve of the capacitor of 6,800 μF. The experimental setup of the WEH powering wireless T&H sensor node is shown in Figure 6B(ii), and the corresponding experimental circuit is shown in Figure S8A. It is worth mentioning that the capacitor that is charged for only 10 s can work as long as 55 s, and a demonstration video is shown in Video S2. On the other hand, a self-powered anemograph is exploited as an IoT sensing node for outdoor appliance in smart buildings. As illustrated in Figure 6C(i), the output of EMG is rectified to charge a supercapacitor of 1.5 F to be used as a power source, and the output of TENG provides AC sensing signals to indicate the wind speed according to the rotating speed of the WEH. The corresponding experimental circuit is shown in Figure S8B. When the rotators turn a full circle, the TENG can generate four complete cycles of AC voltage waveform. That is to say, the frequency of the TENG output waveform can be an available access to obtain the rotation speed of the WEH. Relevant data were measured by an oscilloscope, and the result was depicted in Figure 6C(iii). The frequency of the TENG increases from 2.2 to 29.8 Hz as the wind speed increases from 3.5 to 15 m/s. A systematic test to inspect the accuracy and effectiveness of our anemometer is demonstrated in Video S3, and the experimental setup is shown in Figure 6C(ii). The wind speed is classified into five levels: Calm (<3.5 m/s); Light breeze (3.5–6 m/s); Gentle breeze (6–9 m/s); Fresh breeze (9–12 m/s), and Gale (>12 m/s) according to the meteorological information. During the experiment, the relative position between the WEH and blower remained unchanged and the wind speed was adjusted by a programmable power supply. When the voltage at both ends of the capacitor reached 5 V after charging 20 min by the rectified EMG output, the switch is turned on and the TENG anemograph is charged. Corresponding voltage signal of TENG output was analyzed and processed by Arduino, and eventually the wind speed level was displayed on the computer interface. Considering the capability of powering IoT sensing nodes, the WEH exerts great potential in the application of smart buildings, to provide with temperature, humidity, and wind speed information.

Conclusion

In this article, a novel triboelectric-electromagnetic hybrid WEH based on the revolution and rotation movement of tapered rollers was proposed. Fundamentally, both theoretical model and simulation

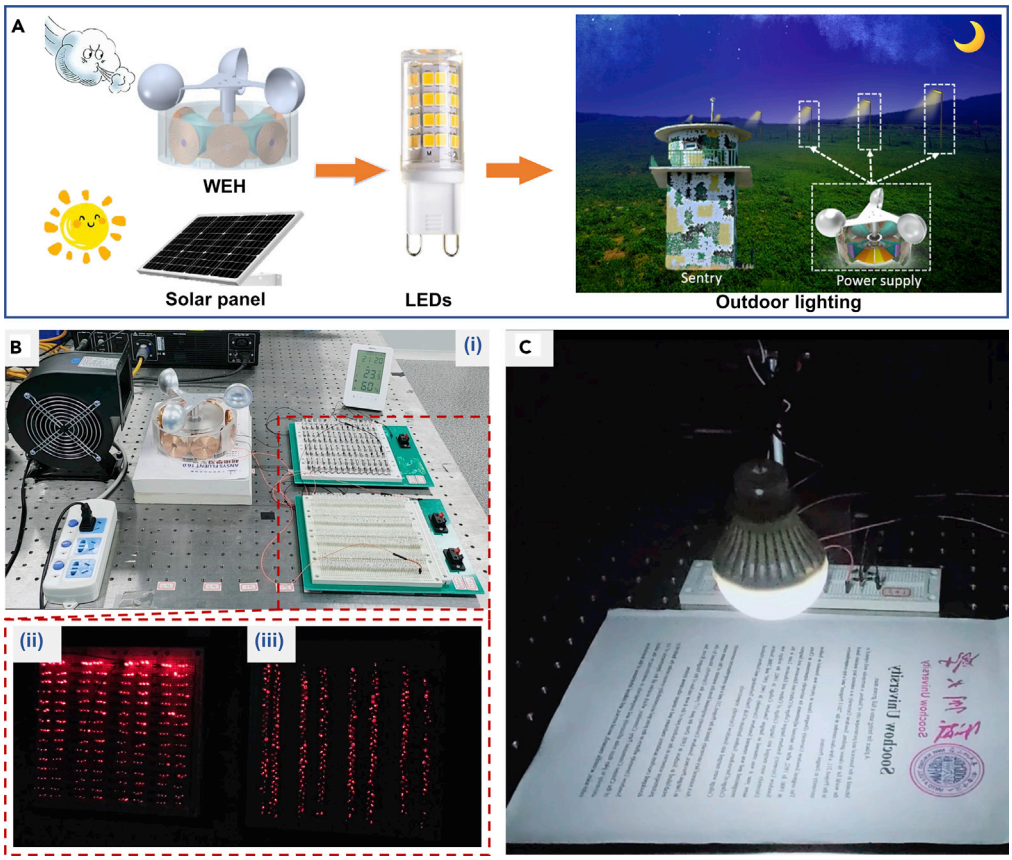

Figure 5. Performance demonstration of the WEH aimed to field lighting application

(A) Schematic illustration of the WEH used as a supplementary power source for wind-solar complementary circuit in field lightening.

(B) Pictures of (i) experimental setup of LED demonstration experiment, (ii) 360 LEDs powered by the EMG, and (iii) 240 LEDs powered by the TENG.

(C) A 5-W globe light supplied by the WEH for reading texts in the darkness.

analysis were carried out, followed by a series of simulated analysis and contrast experiments to optimize the output performance of the EMG and TENG. At the wind speed of 12 m/s, the EMG and TENG of the optimized hybrid WEH can generate the maximum open-circuit voltages of 47.4 and 683 V, respectively. Under the same wind speed, the output power of the EMG reaches the climax of 62 mW at the external load of 660 Ω, which corresponds to a volume output power density of 72.1 W/m^3, whereas the maximum output power of the TENG about 1.8 mW is achieved at the external load of 60 MΩ, which corresponds to a volume output power density of 0.27 W/m^2. A supercapacitor of 1.5 F can be charged to 3 V in 10 min by the EMG, and the TENG can run for ~35,000 cycles continuously without obvious decay. The WEH is demonstrated to power up arrays of LEDs and even a 5-W globe light, which indicates potential talent to be used as a supplementary power source for field lightening. The TENG can also be used as a wind speed sensor by analyzing the output frequency characteristics. Last but not least, combined with corresponding power management circuit, wireless sensor node, and terminal monitoring interface, the device can easily power a wireless environmental monitoring system, such as a wireless temperature and humidity sensing node and a self-powered anemograph, which shows bright application prospects in smart buildings, intelligent agriculture, border detection, and so on.

Methods

Fabrication of the WEH

The WEH, including a rotor, a stator, a driver, and a frame, was mainly fabricated through machining. The device possesses a cylindrical structure with a total dimension of Φ148 mm diameter and 50 mm height.

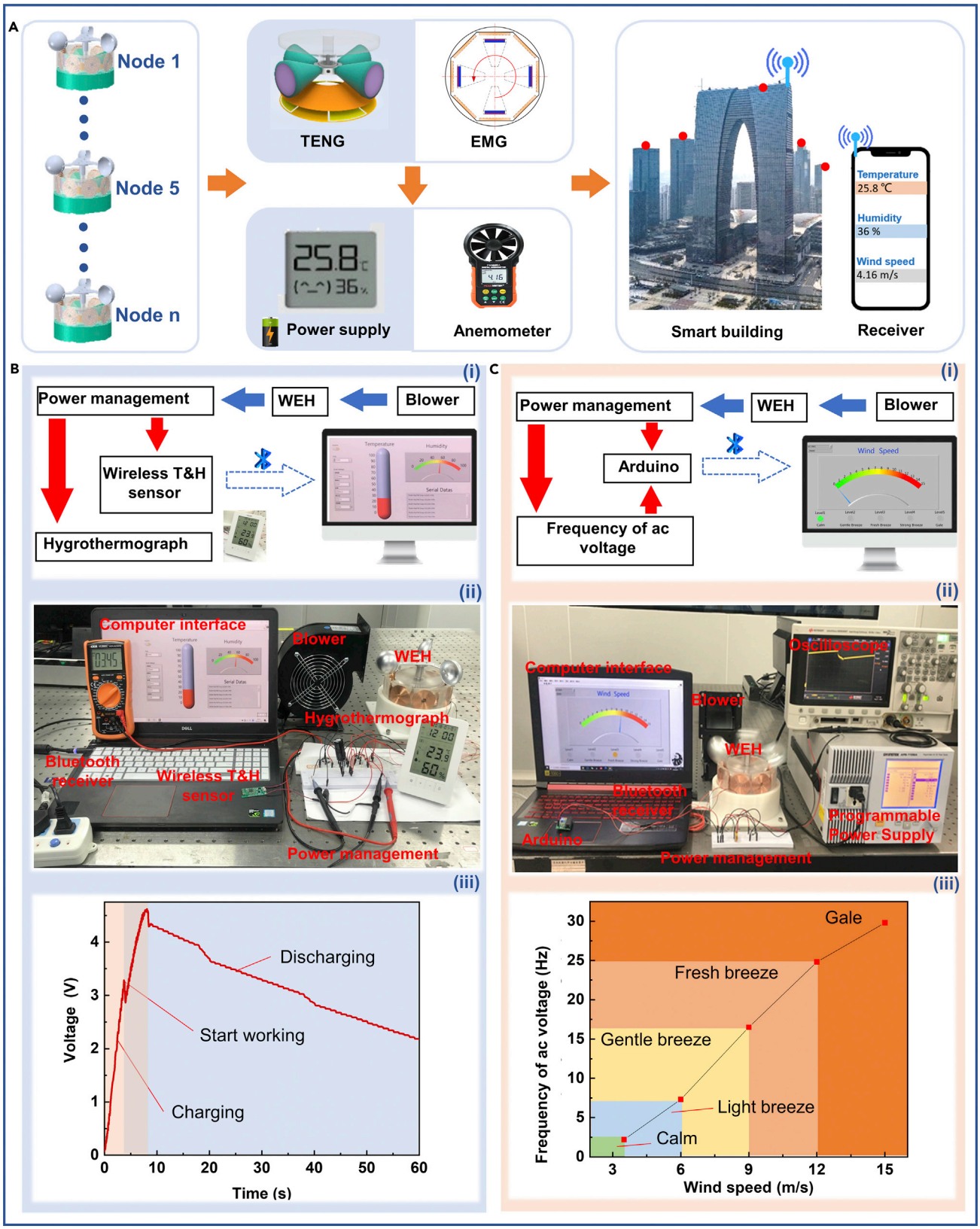
A
Node 1
Node 5
Node n
TENG
EMG
Power supply
Anemometer
Smart building
Receiver
Temperature
25.8 ℃
Humidity
36 %
Wind speed
4.16 m/s
B
(i)
Power management
WEH
Blower
Wireless T&H sensor
Hygrothermograph
(ii)
Computer interface
Blower
WEH
Hygrothermograph
Bluetooth receiver
Wireless T&H sensor
Power management
(iii)
Discharging
Start working
Charging
Voltage (V)
Time (s)
C
(i)
Power management
WEH
Blower
Arduino
Frequency of ac voltage
(ii)
Computer interface
Blower
Oscilloscope
WEH
Bluetooth receiver
Programmable Power Supply
Arduino
Power management
(iii)
Gale
Fresh breeze
Gentle breeze
Light breeze
Calm
Frequency of ac voltage (Hz)
Wind speed (m/s)

Figure 6. Performance demonstration of the WEH aimed to smart building application

(A) Schematic illustration of the WEHs used as the power supplies for IoT nodes in smart buildings.

(B) (i) Working process of the T&H sensing node powered by the WEH; (ii) experimental setup of the WEH powering wireless T&H sensor node; (iii) charging-discharging curve of the 6,800-μF capacitor when powering the hygrothermograph and the T&H sensor node simultaneously.

(C) (i) Working process of the self-powered anemograph; (ii) experimental setup of the self-powered anemograph; (iii) the relationship curve between output frequency of AC voltage of TENG and wind speed.

The rotor is mainly composed of four tapered nylon rollers, four magnets made of NdFeB, and an aluminum mounting ring with four threaded mounting holes. The stator consists of a pair of copper electrodes, a layer of FEP film, and an array of eight copper coils. An Al wind cup acts as the driving part, which connects with a PMMA end cover through an Al shaft anchored in the frame with a ball bearing. The frame is made of PMMA, which has a large tapered plane with high precision to ensure the smoothness of the rotation movement of rotors. The electrodes on the bottom of the stator were prepared by cutting plotter.

Measurement system

The output electric signals (open-circuit voltage, short-circuit current, and transfer charge) of the hybridized WEH were measured by a digital oscilloscope (Keysight DSO3032T), a low-noise current preamplifier (Stanford Research SR570), and a programmable electrometer (Keithley 6514), respectively. The wind was generated by a blower (HK130FLJ5), and an anemometer (Omega HHF11A) was utilized to measure the wind speed. The blower was controlled by a programmable power supply (Gwinstek APS-1102A) to provide different wind speeds.

The electrical potential distribution of the TENG was simulated by the COMSOL Multiphysics software, and the distribution of magnetic flux density of the EMG was simulated by the JMAG software.

METHODS

All methods can be found in the accompanying transparent methods supplemental file.

SUPPLEMENTAL INFORMATION

Supplemental information can be found online at https://doi.org/10.1016/j.isci.2021.102300.

ACKNOWLEDGMENTS

This work is funded by the National Science Foundation of China (Grant No. 51875377).

AUTHORS CONTRIBUTION

Y.F., T.T., and Y.L. contributed equally to this work. H.L. and C.L. designed the studies and revised the manuscript. Y.F., T.T., and Y.L. designed the experiments, analyzed the data, and wrote the paper. Y.F., T.T., Y.L., C.H., and F.W. carried out the experiments, discussed the results, and performed theoretical calculations. Z.Y., L.S., and T.C. discussed and revised the manuscript.

DECLARATION OF INTERESTS

The authors declare no competing interests.

Received: December 26, 2020
Revised: February 19, 2021
Accepted: March 8, 2021
Published: April 23, 2021

REFERENCES

Ahmed, A., Hassan, I., Hedaya, M., Abo El-Yazid, T., Zu, J., and Wang, Z.L. (2017). Farms of triboelectric nanogenerators for harvesting wind energy: a potential approach towards green energy. Nano Energy *36*, 21–29.

Armstrong, R.C., Wolfram, C., de Jong, K.P., Gross, R., Lewis, N.S., Boardman, B., Ragauskas, A.J., Ehrhardt-Martinez, K., Crabtree, G., and Ramana, M.V. (2016). The frontiers of energy. Nat. Energy. *1*, 1–8.

Bansal, A., Howey, D.A., and Holmes, A.S. (2009). CM-scall air turbine and generator for energy harvesting from low-speed flows. Transducers *2009*, 21–25.

Bethi, R.V., Laws, P., Kumar, P., and Mitra, S. (2019). Modified savonius wind turbine for harvesting wind energy from trains moving in tunnels. Renew. Energy *135*, 1056–1063.

Cao, R., Zhou, T., Wang, B., Yin, Y., Yuan, Z., Li, C., and Wang, Z.L. (2017). Rotating-sleeve triboelectric–electromagnetic hybrid

nanogenerator for high efficiency of harvesting mechanical energy. ACS Nano *11*, 8370–8378.

Chen, J., Yang, J., Guo, H., Li, Z., Zheng, L., Su, Y., Wen, Z., Fan, X., and Al, C.E.T. (2015a). Automatic mode transition enabled robust triboelectric nanogenerators. ACS Nano *12*, 12334–12343.

Chen, J.J., Symes, M.D., Fan, S.C., Zheng, M.S., Miras, H.N., Dong, Q.F., and Cronin, L. (2015b). High-performance polyoxometalate-based cathode materials for rechargeable lithium-ion batteries. Adv. Mater. *27*, 4649–4654.

Chen, S., Gao, C., Tang, W., Zhu, H., Han, Y., Jiang, Q., Li, T., Cao, X., and Wang, Z. (2015c). Self-powered cleaning of air pollution by wind driven triboelectric nanogenerator. Nano Energy *14*, 217–225.

Chen, T., Xia, Y., Liu, W., Liu, H., Sun, L., and Lee, C. (2016). A hybrid flapping-blade wind energy harvester based on vortex shedding effect. J. Microelectromech. Syst. *25*, 845–847.

Chen, T., Zhao, M., Shi, Q., Yang, Z., Liu, H., Sun, L., Ouyang, J., and Lee, C. (2018). Novel augmented reality interface using a self-powered triboelectric based virtual reality 3D-control sensor. Nano Energy *51*, 162–172.

Chen, T., Shi, Q., Zhu, M., He, T., Yang, Z., Liu, H., Sun, L., Yang, L., and Lee, C. (2019). Intuitive-augmented human-machine multidimensional nano-manipulation terminal using triboelectric stretchable strip sensors based on minimalist design. Nano Energy *60*, 440–448.

Chen, X., Gao, L., Chen, J., Lu, S., Zhou, H., Wang, T., Wang, A., Zhang, Z., Guo, S., Mu, X., et al. (2020). A chaotic pendulum triboelectric-electromagnetic hybridized nanogenerator for wave energy scavenging and self-powered wireless sensing system. Nano Energy *69*, 104440.

Cheng, M., and Zhu, Y. (2014). The state of the art of wind energy conversion systems and technologies: a review. Energy Convers. Manage. *88*, 332–347.

Cheng, T., Gao, Q., and Wang, Z.L. (2019). The current development and future outlook of triboelectric nanogenerators: a survey of literature. Adv. Mater. Technol. *4*, 1800588.

Chu, S., and Majumdar, A. (2012). Opportunities and challenges for a sustainable energy future. Nature *488*, 294–303.

El-Askary, W.A., Nasef, M.H., AbdEl-hamid, A.A., and Gad, H.E. (2015). Harvesting wind energy for improving performance of savonius rotor. J. Wind Eng. Ind. Aerod *139*, 8–15.

Fan, X., He, J., Mu, J., Qian, J., Zhang, N., Yang, C., Hou, X., Geng, W., Wang, X., and Chou, X. (2020). Triboelectric-electromagnetic hybrid nanogenerator driven by wind for self-powered wireless transmission in Internet of things and self-powered wind speed sensor. Nano Energy *68*, 104319.

Fei, F., Mai, J.D., and Li, W.J. (2012). A wind-flutter energy converter for powering wireless sensors. Sens. Actuators, A. *173*, 163–171.

Fu, H., and Yeatman, E.M. (2015a). A miniature radial-flow wind turbine using piezoelectric transducers and magnetic excitation. J. Phys. Conf. Ser. *660*, 012058.

Fu, H., and Yeatman, E.M. (2015b). A miniaturized piezoelectric turbine with self-regulation for increased air speed range. Appl. Phys. Lett. *107*, 243905.

Guo, H., Wen, Z., Zi, Y., Yeh, M.-H., Wang, J., Zhu, L., Hu, C., and Wang, Z.L. (2016). A water-proof triboelectric-electromagnetic hybrid generator for energy harvesting in harsh environments. Adv. Energ. Mater. *6*, 1–7.

Guo, Y., Chen, Y., Ma, J., Zhu, H., Cao, X., Wang, N., and Wang, Z.L. (2019). Harvesting wind energy: a hybridized design of pinwheel by coupling triboelectrification and electromagnetic induction effects. Nano Energy *60*, 641–648.

Halim, M.A., Rantz, R., Zhang, Q., Gu, L., Yang, K., and Roundy, S. (2018). An electromagnetic rotational energy harvester using sprung eccentric rotor, driven by pseudo-walking motion. Appl. Energy. *217*, 66–74.

Hao, C., He, J., Zhai, C., Jia, W., Song, L., Cho, J., Chou, X., and Xue, C. (2019). Two-dimensional triboelectric-electromagnetic hybrid nanogenerator for wave energy harvesting. Nano Energy *58*, 147–157.

He, J., Cao, S., and Zhang, H. (2019). Cylinder-based hybrid rotary nanogenerator for harvesting rotational energy from axles and self-powered tire pressure monitoring. Energy Sci. Eng. *8*, 291–299.

Hou, C., Chen, T., Li, Y., Huang, M., Shi, Q., Liu, H., Sun, L., and Lee, C. (2019). A rotational pendulum based electromagnetic/triboelectric hybrid-generator for ultra-low-frequency vibrations aiming at human motion and blue energy applications. Nano Energy *63*, 103871.

Kim, D., Tcho, I.-W., and Choi, Y.-K. (2018). Triboelectric nanogenerator based on rolling motion of beads for harvesting wind energy as active wind speed sensor. Nano Energy *52*, 256–263.

Kosunalp, S. (2017). An energy prediction algorithm for wind-powered wireless sensor networks with energy harvesting. Energy *139*, 1275–1280.

Lai, Y.C., Hsiao, Y.C., Wu, H.M., and Wang, Z.L. (2019). Waterproof fabric-based multifunctional triboelectric nanogenerator for universally harvesting energy from raindrops, wind, and human motions and as self-powered sensors. Adv. Sci. (Weinh). *6*, 1801883.

Li, S., and Lipson, H. (2009). Vertical-stalk flapping-leaf generator for wind energy harvesting. Asme Conf. Smart Mater. *2*, 611–619.

Li, Y., Cheng, G., Lin, Z.-H., Yang, J., Lin, L., and Wang, Z.L. (2015). Single-electrode-based rotationary triboelectric nanogenerator and its applications as self-powered contact area and eccentric angle sensors. Nano Energy *11*, 323–332.

Li, J., Gu, W., and Yuan, H. (2016). Research on IOT technology applied to intelligent agriculture. Proceedings of the 5th international conference on electrical engineering and automatic control. Lecture Notes Electr. Eng. *367*, 1217–1224.

Li, Y., Guo, Q., Huang, M., Ma, X., Chen, Z., Liu, H., and Sun, L. (2019). Study of an electromagnetic ocean wave energy harvester driven by an efficient swing body toward the self-powered ocean buoy application. IEEE Access *7*, 129758–129769.

Lin, L., Wang, S., Xie, Y., Jing, Q., Niu, S., Hu, Y., and Wang, Z.L. (2013). Segmentally structured disk triboelectric nanogenerator for harvesting rotational mechanical energy. Nano Lett. *13*, 2916–2923.

Lin, L., Wang, S., Niu, S., Liu, C., Xie, Y., and Wang, Z.L. (2014). Noncontact free-rotating disk triboelectric nanogenerator as a sustainable energy harvester and self-powered mechanical sensor. ACS Appl. Mater. Interfaces *6*, 3031–3038.

Lin, H., He, M., Jing, Q., Yang, W., Wang, S., Liu, Y., Zhang, Y., Li, J., Li, N., Ma, Y., et al. (2019). Angle-shaped triboelectric nanogenerator for harvesting environmental wind energy. Nano Energy *56*, 269–276.

Liu, H., Xia, Y., Chen, T., Yang, Z., Liu, W., Wang, P., and Sun, L. (2017). Study of a hybrid generator based on triboelectric and electromagnetic mechanisms. IEEE Sens. J. *17*, 3853–3860.

Liu, K., Yu, M., and Zhu, W. (2019). Enhancing wind energy harvesting performance of vertical Axis wind turbines with a new hybrid design: a fluid-structure interaction study. Renew. Energy *140*, 912–927.

Liu, H., Zhong, J., Lee, C., Lee, S.W., and Lin, L. (2018). A comprehensive review on piezoelectric energy harvesting technology: materials, mechanisms, and applications. Appl. Phys. Rev. *5*, 041306.

Oh, J., Yuan, H.C., and Branz, H.M. (2012). An 18.2%-efficient black-silicon solar cell achieved through control of carrier recombination in nanostructures. Nat. Nanotechnol. *7*, 743–748.

Orrego, S., Shoele, K., Ruas, A., Doran, K., Caggiano, B., Mittal, R., and Kang, S.H. (2017). Harvesting ambient wind energy with an inverted piezoelectric flag. Appl. Energy. *194*, 212–222.

Ryu, H., Yoon, H.J., and Kim, S.W. (2019). Hybrid energy harvesters: toward sustainable energy harvesting. Adv. Mater. *31*, 1802898.

Spreemann, D., Manoli, Y., Folkmer, B., and Mintenbeck, D. (2006). Non-resonant vibration conversion. J. Micromech. Microeng. *16*, S169–S173.

Wang, Z.L. (2013). Triboelectric nanogenerators as new energy technology for self-powered systems and as active mechanical and chemical sensors. ACS Nano *7*, 24.

Wang, S., Lin, L., and Wang, Z.L. (2012). Nanoscale triboelectric-effect-enabled energy conversion for sustainably powering portable electronics. Nano Lett. *12*, 6339–6346.

Wang, X., Pan, C.L., Liu, Y.B., and Feng, Z.H. (2014). Electromagnetic resonant cavity wind energy harvester with optimized reed design and effective magnetic loop. Sens. Actuators, A. *205*, 63–71.

Wang, S., Lin, L., and Wang, Z.L. (2015). Triboelectric nanogenerators as self-powered active sensors. Nano Energy *11*, 436–462.

Wang, S., Wang, X., Wang, Z.L., and Yang, Y. (2016). Efficient scavenging of solar and wind energies in a smart city. ACS Nano *10*, 5696–5700.

Wang, Y., Wang, J., Xiao, X., Wang, S., Kien, P.T., Dong, J., Mi, J., Pan, X., Wang, H., and Xu, M. (2020). Multi-functional wind barrier based on triboelectric nanogenerator for power generation, self-powered wind speed sensing and highly efficient windshield. Nano Energy *73*, 104736.

Michael A. Weimer, T.S.P., Regan A. Zane, (2006). Remote Area Wind Energy Harvesting for Low-Power Autonomous Sensors. Power Electronics Specialists Conference2006.

Weinstein, L.A., Cacan, M.R., So, P.M., and Wright, P.K. (2012). Vortex shedding induced energy harvesting from piezoelectric materials in heating, ventilation and air conditioning flows. Smart Mater. Struct. *21*, 045003.

Wen, Z., Chen, J., Yeh, M.-H., Guo, H., Li, Z., Fan, X., Zhang, T., Zhu, L., and Wang, Z.L. (2015). Blow-driven triboelectric nanogenerator as an active alcohol breath analyzer. Nano Energy *16*, 38–46.

Wen, Z., Guo, H., Zi, Y., Yeh, M.H., Wang, X., Deng, J., Wang, J., Li, S., Hu, C., Zhu, L., and Wang, Z.L. (2016). Harvesting broad frequency band blue energy by a triboelectric-electromagnetic hybrid nanogenerator. ACS Nano *10*, 6526–6534.

Xie, Y., Wang, S., Lin, L., Jing, Q., Lin, Z.-h., Niu, S., and Wu, Z. (2013). Rotary triboelectric nanogenerator based on a hybridized mechanism for harvesting wind energy. ACS Nano *8*, 7119–7125.

Yang, H., Liu, W., Xi, Y., Lai, M., Guo, H., Liu, G., Wang, M., Li, T., Ji, X., and Li, X. (2018). Rolling friction contact-separation mode hybrid triboelectric nanogenerator for mechanical energy harvesting and self-powered multifunctional sensors. Nano Energy *47*, 539–546.

Yang, H., Wang, M., Deng, M., Guo, H., Zhang, W., Yang, H., Xi, Y., Li, X., Hu, C., and Wang, Z. (2019). A full-packaged rolling triboelectric-electromagnetic hybrid nanogenerator for energy harvesting and building up self-powered wireless systems. Nano Energy *56*, 300–306.

Zhang, C., Tang, W., Han, C., Fan, F., and Wang, Z.L. (2014). Theoretical comparison, equivalent transformation, and conjunction operations of electromagnetic induction generator and triboelectric nanogenerator for harvesting mechanical energy. Adv. Mater. *26*, 3580–3591.

Zhang, C., He, X.F., Li, S.Y., Cheng, Y.Q., and Rao, Y. (2015). A wind energy powered wireless temperature sensor node. Sensors (Basel). *15*, 5020–5031.

Zhang, B., Chen, J., Jin, L., Deng, W., Zhang, L., Zhang, H., Zhu, M., Yang, W., and Wang, Z.L. (2016). Rotating-disk-based hybridized electromagnetic–triboelectric nanogenerator for sustainably powering wireless traffic volume sensors. ACS Nano *10*, 6241–6247.

Zhang, J., Fang, Z., Shu, C., Zhang, J., Zhang, Q., and Li, C. (2017). A rotational piezoelectric energy harvester for efficient wind energy harvesting. Sens. Actuators A. *262*, 123–129.

Zhao, Z., Pu, X., Du, C., Li, L., Jiang, C., Hu, W., and Wang, Z.L. (2016). Freestanding flag-type triboelectric nanogenerator for harvesting high-altitude wind energy from arbitrary directions. ACS Nano *10*, 1780–1787.

Zhao, C., Zhang, Q., Zhang, W., Du, X., Zhang, Y., Gong, S., Ren, K., Sun, Q., and Wang, Z.L. (2019a). Hybrid piezo/triboelectric nanogenerator for highly efficient and stable rotation energy harvesting. Nano Energy *57*, 440–449.

Zhao, J., Zhen, G., Liu, G., Bu, T., Liu, W., Fu, X., Zhang, P., Zhang, C., and Wang, Z.L. (2019b). Remarkable merits of triboelectric nanogenerator than electromagnetic generator for harvesting small-amplitude mechanical energy. Nano Energy *61*, 111–118.

Zheng, L., Lin, Z.H., Cheng, G., Wu, W., Wen, X., Lee, S., and Wang, Z.L. (2014). Silicon-based hybrid cell for harvesting solar energy and raindrop electrostatic energy. Nano Energy *9*, 291–300.

Zhong, X., Yang, Y., Wang, X., and Wang, Z.L. (2015). Rotating-disk-based hybridized electromagnetic-triboelectric nanogenerator for scavenging biomechanical energy as a mobile power source. Nano Energy *13*, 771–780.

Zhou, Z., Qin, W., Zhu, P., and Shang, S. (2018). Scavenging wind energy by a Y-shaped Bi-stable energy harvester with curved wings. Energy *153*, 400–412.

iScience, Volume *24*

Supplemental information

A high-performance triboelectric-electromagnetic hybrid wind energy harvester based on rotational tapered rollers aiming at outdoor IoT applications

Yan Fang, Tianyi Tang, Yunfei Li, Cheng Hou, Feng Wen, Zhan Yang, Tao Chen, Lining Sun, Huicong Liu, and Chengkuo Lee

Supporting Information for

A high-performance triboelectric–electromagnetic hybrid wind energy harvester based on rotational tapered rollers aiming at outdoor IoT applications

Yan Fang[1,6],Tianyi Tang[1,6], Yunfei Li [2,6], Cheng Hou[1], Feng Wen[3,4,5], Zhan Yang [1,*] Tao Chen[1], Lining Sun[1], Huicong Liu[1,7,*], and Chengkuo Lee[3,4,5,*]

[1]School of Mechanical and Electric Engineering, Jiangsu Provincial Key Laboratory of Advanced Robotics, Soochow University, Suzhou 215123, China

[2]State Key Laboratory of Robotics and System, Harbin Institute of Technology (HIT), Harbin 150001, China

[3]Department of Electrical & Computer Engineering, National University of Singapore, 4 Engineering Drive 3, Singapore, 117576, Singapore

[4]National University of Singapore Suzhou Research Institute (NUSRI), Suzhou Industrial Park, Suzhou, 215123, China

[5]Center for Intelligent Sensors and MEMS, National University of Singapore, E6 #05-11F, 5 Engineering Drive 1, Singapore, 117608, Singapore

[6] These authors contribute equally to this work.

[7] Lead contact

* Correspondence: hcliu078@suda.edu.cn (H.L.), yangzhan@suda.edu.cn (Z.Y.), elelc@nus.edu.sg (C.L.)

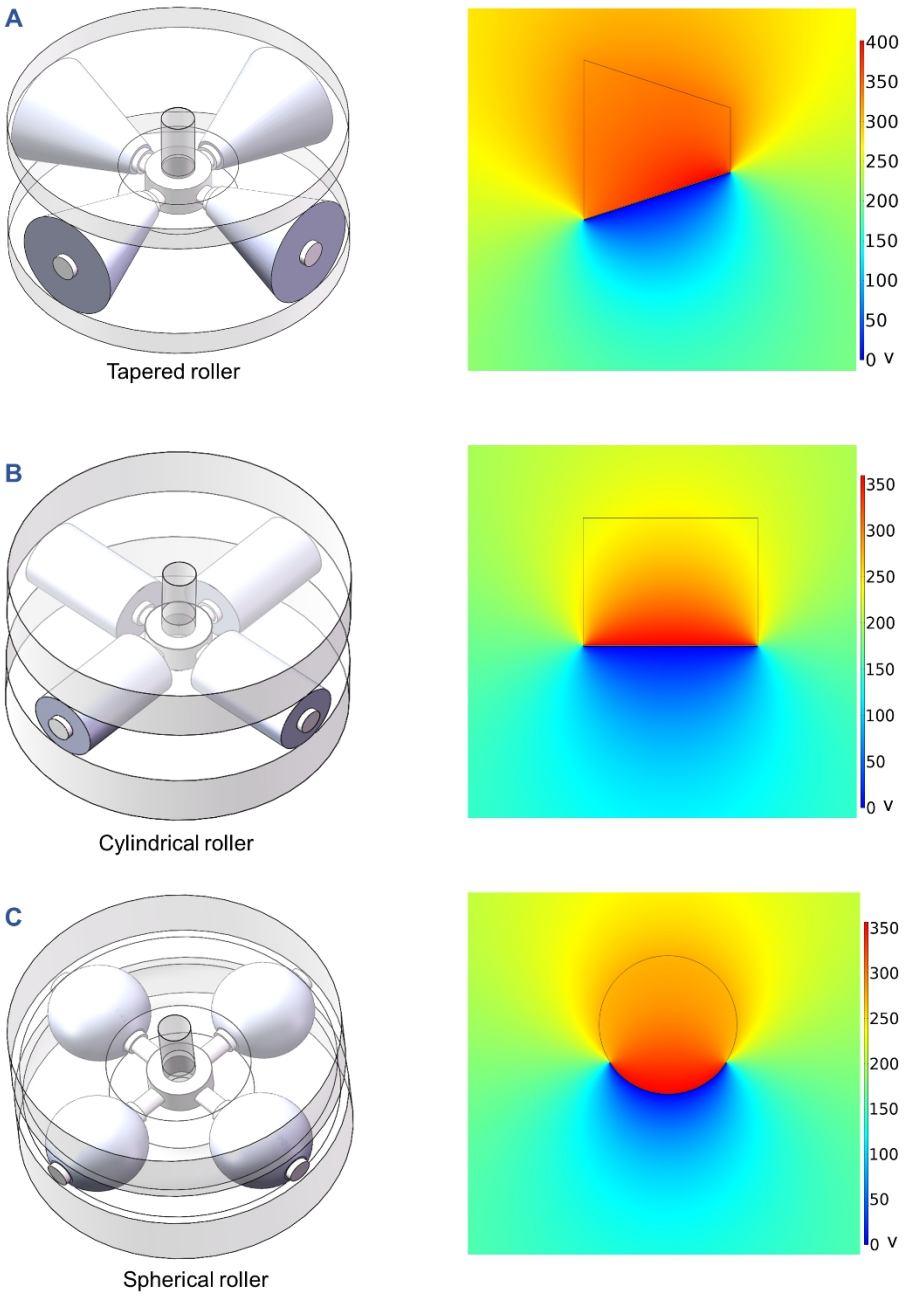

Figure S1. The potential distribution between the electrodes of TENG with different roller shapes, Related to Figure 1.

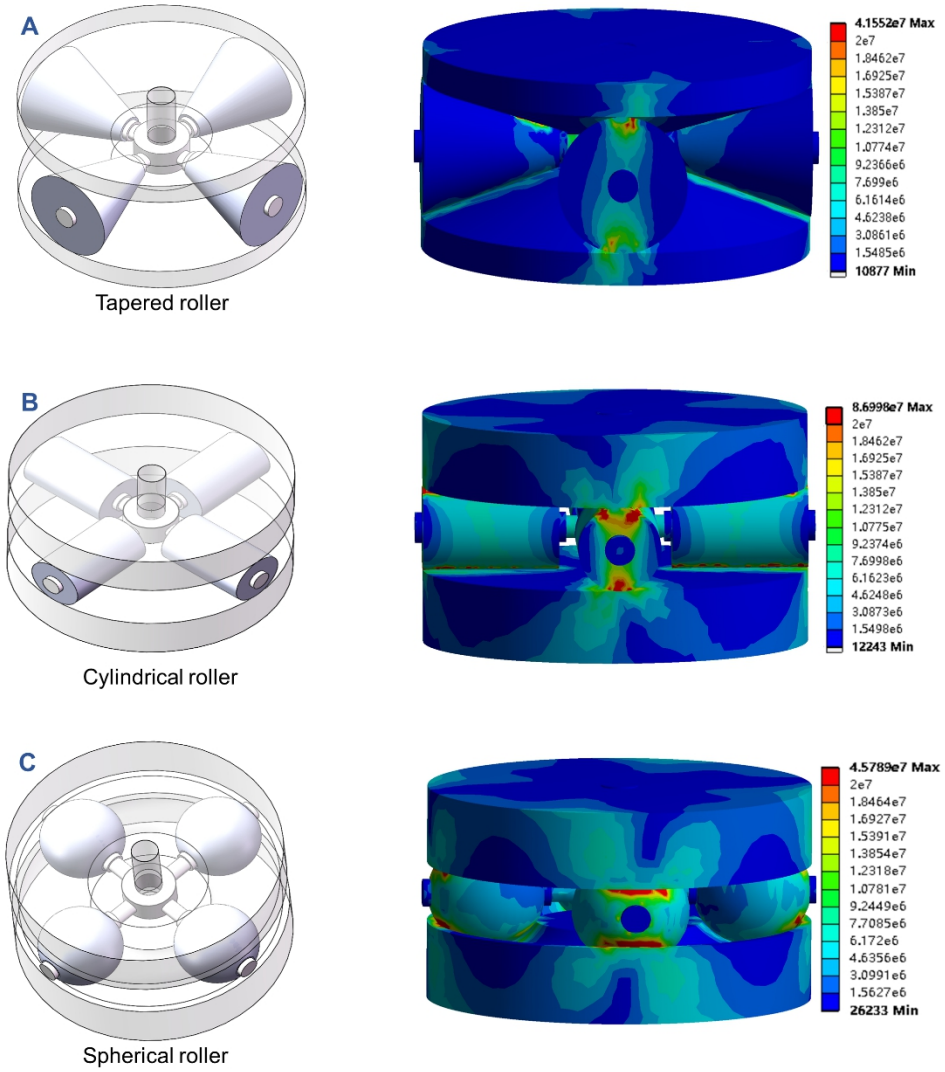

Figure S2. The distribution of equivalent stress of different roller shapes, Related to Figure 1.

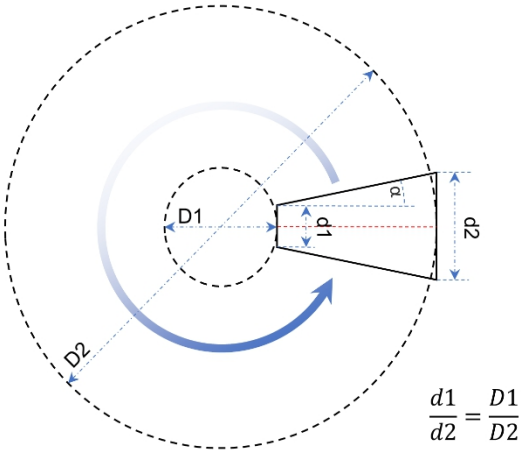

Figure S3. The design parameters of the tapered roller, Related to Figure 1.

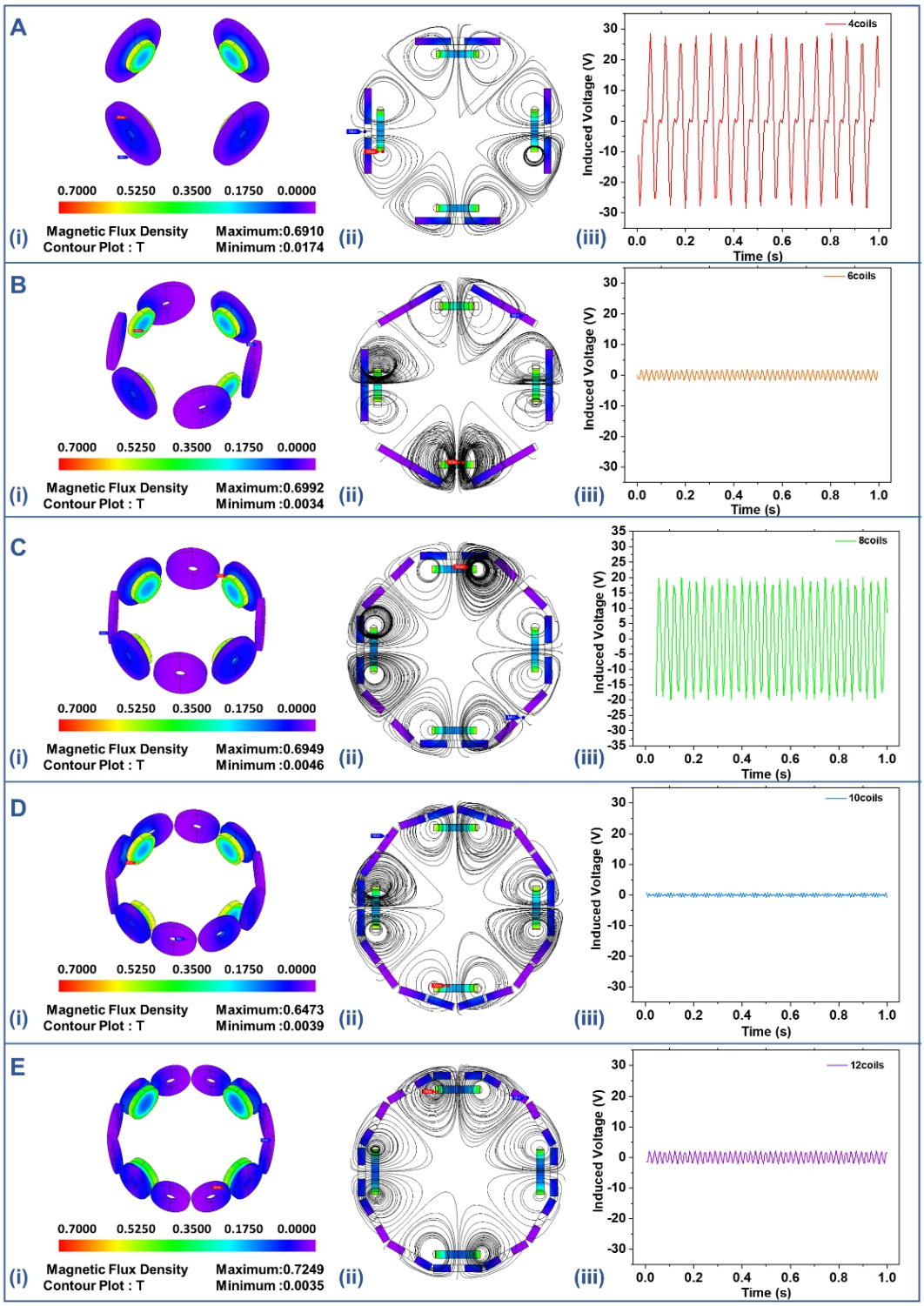

Figure S4. Numerical calculation results of the EMG with different numbers of coils, Related to Figure 2.

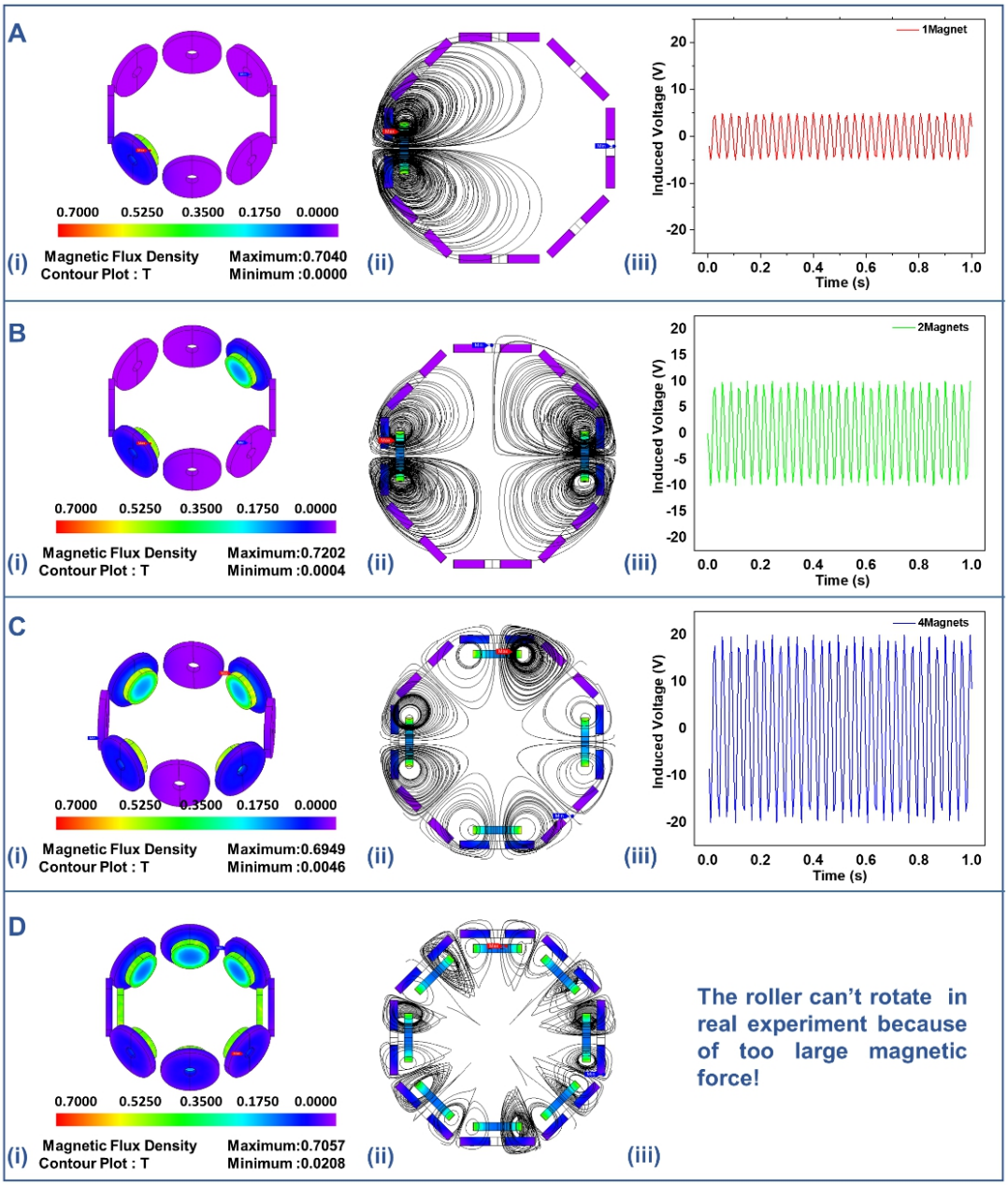

Figure S5. Numerical calculation results of the EMG with different numbers of magnets, Related to Figure 2.

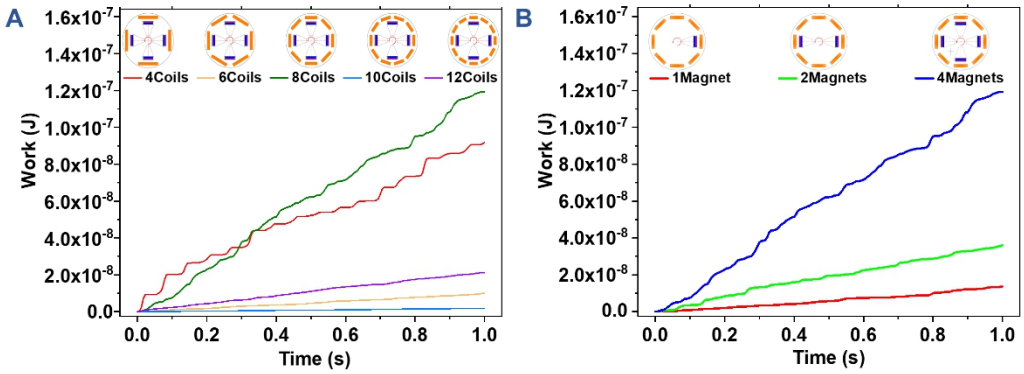

Figure S6. The numerical calculation results of average output power with different numbers of coils and different numbers of magnets, Related to Figure 2.

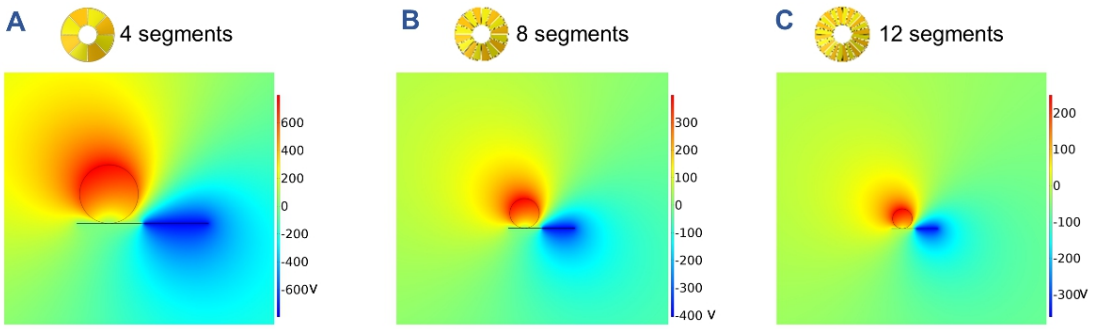

Figure S7. The potential distribution of the TENG with different size of tapered rollers and different segments of electrodes, Related to Figure 3.

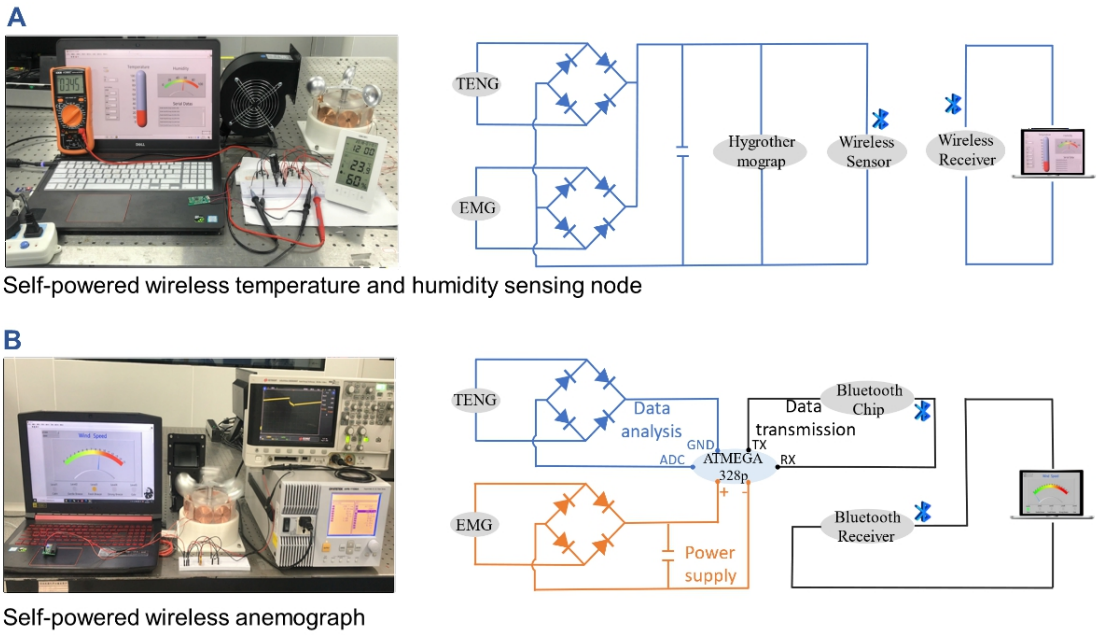

Figure S8. The power management circuit diagram, Related to Figure 6.